Application of a Microfocus X-Ray Imaging Apparatus to the Study of Cellular Polymers

E. Solórzano[1, 2], J. Pinto[2], S. Pardo[2], M.A. Rodriguez-Perez[2], F.Garcia-Moreno[1]

[1] *Institute of Applied Materials, Helmholtz-Centre Berlin, Hahn-Meitner-Platz 1, D-14109 Berlin, Germany.*

[2] *Cellular Materials Laboratory (**C**ell**M**at), Condensed Matter Physics Department, University of Valladolid, 47011 Valladolid, Spain.*

Corresponding e-mail: marrod@fmc.uva.es

Abstract:

Present work reports an X-ray based non-destructive imaging method to study diverse types of polymer foams. A wide description of the main hardware elements –tube and detector, specially adapted for low X-ray absorbing materials– is provided. Recommendations on the optimum imaging parameters for polymer foams are also reported. The mathematical equations and methodology to obtain fine quantitative density information from the images are extensively explained, providing further discussion on the limitations and resolution of such technique. Most of potential applications aimed at studying polymer foams are summarized at the end of this work.

Introduction

Non-Destructive testing (NDT) comprises a wide group of analysis techniques used in science and industry to evaluate the properties of a material, component or system without causing damage [1]. The terms Non-Destructive Examination/Evaluation (NDE) and Non-Destructive Inspection (NDI) are also commonly used to describe these methods [2]. Because NDT does not alter the article being inspected, it is a highly-valuable technique that permits saving both money and time in product evaluation, troubleshooting and research. Common NDT methods include vibration analysis, infrared thermography, acoustic emission analysis, ultrasonic imaging, X-ray computed tomography, digital radiography, ground penetrating radar, optical testing methods, magnetic-particle, penetrating liquids, gammagraphy, eddy-current testing, and low coherence interferometry [2], among others.

Since the 1920s, NDT has progressively developed from a laboratory curiosity to a powerful tool for scientist and manufacturers. Modern nondestructive X-ray imaging is used by manufacturers to ensure product integrity and reliability, to improve product design and to provide in-line manufacturing control [3]. Alternatively, from the scientific point of view, X-ray imaging techniques in materials science are becoming more and more important since the early 1990's and time and spatial resolution are, nowadays, beyond the microscale level [4] . In the particular case of polymer foams, one of the most common nondestructive method used by scientists to characterize these materials is X-ray microtomography [5-10]. This ex-situ characterization method allows obtaining a detailed analysis of the internal architecture of the foam, which permits obtaining information both in the mesoscale (density profiles and presence of large defects) and in the microscale (cell size, cell wall thickness, anisotropy, etc). However, this powerful X-ray method has the main limitation of the relatively high scanning time required to obtain a high resolution 3D image that makes extremely difficult to perform real-time experiments with time resolutions of a few seconds, although this is only achievable under very special conditions [11].

In contrast, the alternative use of 2D X-ray imaging (radiography) and time resolved X-ray imaging (radioscopy) can be complementary useful for the study of this type of materials ex-situ or either in-situ, respectively. Due to the small size of structures intended to be resolved (cell walls of thickness of few microns) this technique necessarily involves the use of high resolution detectors and micro/nanofocus sources. This versatile technique enables observing structural details within specimens, by encoding in its 2D projection the spatial variations in specimen's density and atomic number though their transmitted intensities.

In-situ analysis of the foaming behaviour of cellular plastics appeared in previous decades and with special mention in the last ten years. Different experimental challenges have to be considered depending of the type of base material: thermoset or thermoplastic. In the case of thermosets -usually foamed at room temperature and atmospheric pressure- the experimental set-up is simpler [12-15] than that needed for thermoplastic foams, foamed at higher temperatures. In this particular case thermo-mechanical analysis [16,17] and optical expandometry [18] techniques have been used. Advanced approaches to in-situ examine the foamability of thermoplastics in autoclaves by optical methods have been recently done [19]. Nevertheless, no any in-situ analysis of polymer foam evolution during its production by means of X-ray radioscopy has been found in the literature. Actually, apart from X-ray tomography imaging, only Cunningham [20] evaluated the potential of X-rays radiography for the study of polymer foams and composites by film-radiography showing diverse examples. Even he showed a few in-situ X-ray images of the creep behaviour in presence of external pressure.

In contrast to previously done within the polymer foams field, X-ray radioscopy has been revealed as a powerful technique to examine the foaming behaviour of aluminium foams considering the advantage of monitoring the internal evolution of the cellular structure. The first successful results were obtained using synchrotron radioscopy in the early 2000 [21, 22]. With this experience, a microfocus X-ray laboratory facility was built with the objective of providing a deeper knowledge on these metallic cellular materials [23]. The use of this type of systems has permitted obtaining a better understanding of the main phenomena occurring during foaming in these materials [24-29].

Taking into account that there is a need for a better understanding of the foaming mechanisms in polymeric foams an X-ray imaging system allowing the visualization of the internal structure of the polymer foam during growing with high contrast, spatial and time resolution could be very helpful from the scientific point of view, as previous studies in metallic foams have shown. The low density of polymers and, as a consequence, the low contrast in X-ray imaging for these materials makes the development of this system a challenge from the technical point of view.

Bearing the previous ideas in mind, a new X-ray radioscopy device specifically designed for the non-destructive testing of polymer based foams have been designed and built. This paper presents for first time the technical requirements, the final design and the optimum operation parameters of this novel system. Moreover a detailed analysis of the apparent thickness increase due to cone beam geometry is presented here for first time. The method for density determination is exhaustively

explained and companied with an error analysis. In the final part an outlook on the possibilities of this technique is provided.

2. Experimental techniques

2.1. Hardware description and mode of operation

The constructed microfocal X-ray equipment consists basically in two main elements. A closed, air-cooled microfocus X-ray source from Hamamatsu, Japan, is used to produce the X-rays (focal spot size: 5-20 μm, voltage: 20-100 kV, current: 0-200 μA,) with a maximum output power of 20 W. Complementarily a flat panel (FP) detector from Hamamatsu, Japan, in combination with a frame grabber, Dalsa-Coreco, USA, provides the digital X-ray images. The high resolution detector is composed by a matrix of 2240 x 2344 pixels^2 with a pixel size of 50 μm, i.e. sizing 120 x 120 mm^2 aprox. Digital output is a 12 bits depth resolution with an imaging capacity up to 9fps at maximum acquisition velocity. Dedicated software from Hamamatsu (HiPic) is used to control the acquisition and storing the images.

X-rays within the source are produced by an ultrafine electron beam, striking on a tungsten target in high vacuum atmosphere. The tungsten target produces X-rays when impacted by electrons, thus defining the so-called microfocal spot size in the X-rays origin. The X-rays come out the source through a Beryllium 150μm-thick window forming an X-ray cone beam of 39º for this particular tube. Characteristic spot size of 5μm trends to slightly broaden if electron acceleration voltage or current are increased up to a maximum of 20 μm; below 40% of maximum power spot size keeps in its smaller size.

Flat panel (FP) detector technology essentially consists on a combination of deposited scintillator material (CsI, GOS, Se, etc) layer in front of a CMOS detector. One of its main advantages yields in the small dimensions of the complete high resolution imaging apparatus compared to traditional combinations of scintillator, optical system and camera.

It is important to remark that the selection of both the X-ray tube and the detector had to be done with special care, considering that polymers are low absorbing materials and the need of sufficient soft X-rays to provide optimum contrast in the final image. In this sense, the source was selected in regard to its combination of small spot size (related to final spatial resolution as we will comment in next sections) and low minimum X-ray output energy (kV) compared to other types. On the other hand, the particular detector selected consisted in a custom-made *direct deposition* of CsI (scintillator material) on the CMOS surface. Direct deposition technology improves the efficiency by collecting in the CMOS detector a higher amount of light produced in the scintillator, in

comparison with other FP technologies in which scintillator is deposited on other substrate and there is a gap in between it and the CMOS. This particular type of FP detector is covered by a 1 mm-thick carbon fibre plate, thus reducing the X-ray absorption as much as possible. Commonly, most of detectors are designed for relatively high energies and, as their kV-response curve is not linear, it's hard to obtain high-quality images at low energies. Eventually, some detectors produce a significant response, even for high tube intensities and/or high detector exposure times, only over a certain threshold minimum X-ray energy. Nevertheless, the custom FP detector used presented significant response at comparative lower energies. Figure 1 shows the comparative response of high sensibility custom detector used in the present equipment compared with a conventional detector (mod. C7942) showing that the signal covers a higher dynamic range (%DR) in smaller energy range.

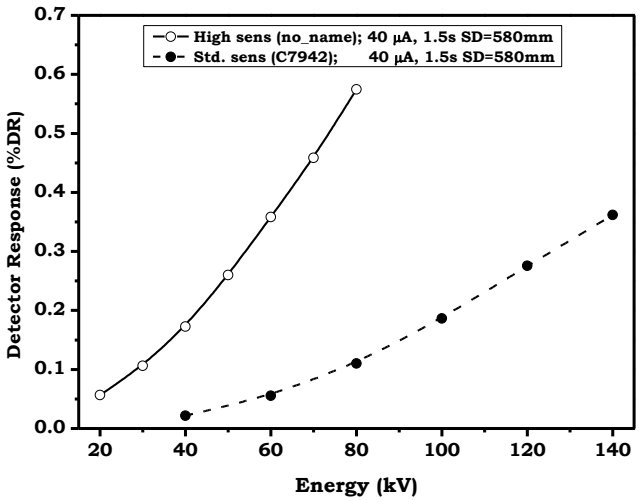

Figure 1. Comparative response of different X-ray flat panels.
(●) standard sensibility detector, C7942; (○) high sensibility detector

Both main elements are settled, one in front of each other, as described in fig. 2. In principle it is possible to position them at any source to the detector distance (*SD)*, but in general optimum distances are in the range of 0.3 to 1.2 m. As the beam is cone-spread the more distance the less radiation the FP-detector receives, what, in principle, is positive for its lifetime but reduces image quality since different perturbing effects increase with distance, as it will be explained in following sections. In this particular set up, distance chosen has been 600 mm, becoming a compromise distance for all the involved factors.

The object to be X-ray-monitored is located at any position in between the detector and the source. The fact of having a diverging X-ray beam allows for object magnification. Magnification factor, *M*, is a function of the object to source distance, *OS*, compared to *SD*. Thus magnification is defined as:

$$M = \frac{OS}{SD} \tag{1}$$

In a first approach, pixel resolution is the result of dividing the pixel size by the magnification factor, although some other facts need to be considered in order to calculate the real resolution. Objects to be examined can be, in principle, of any size. Nevertheless the maximum size depends on the magnification factor and on the total detector's active area (aprox. 120 x 120 mm^2). Thus maximum field of view (at $M = 1$) corresponds to the active area and it reduces with magnification in consonance with pixel resolution. Object thickness (in the direction of the X-rays) also influences the image as it will be commented in next section.

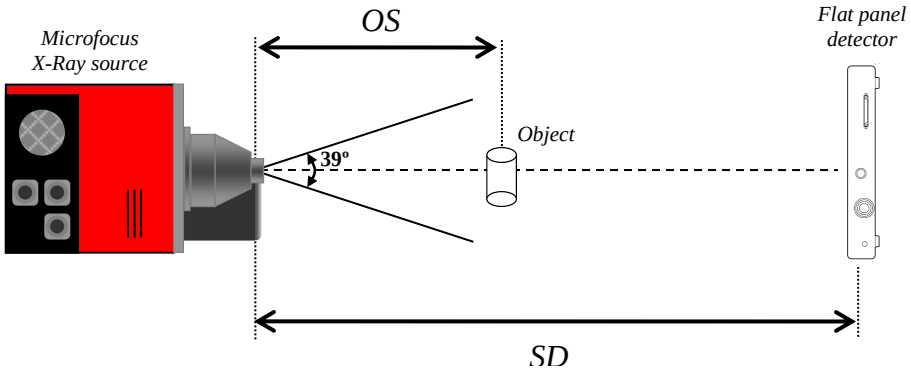

Figure 2. Schematic draw of the high resolution X-ray imaging system

2.2. Spatial, temporal and contrast resolution

Previously defined magnification, *M*, presents certain optical limits due to the finite size of both the focal spot, *F*, and the pixel size, P_s. Finite size of the focal spot is responsible for the not well defined edges of the visualized object, presenting a characteristic apparent density gradient in the object edges (penumbra region). Similarly, digitalization by means of a detector with finite pixel size limits the spatial frequency, *f*. Therefore, optical resolution limits for this particular X-ray set-up are determined by the cut-off frequency (f_c in figure 3). The cut-off frequency is defined as the

value in which the two equations describing the resolution of the two systems reach the same value, as shown in figure 3. This cut-off frequency determines the maximum magnification (M_{max})

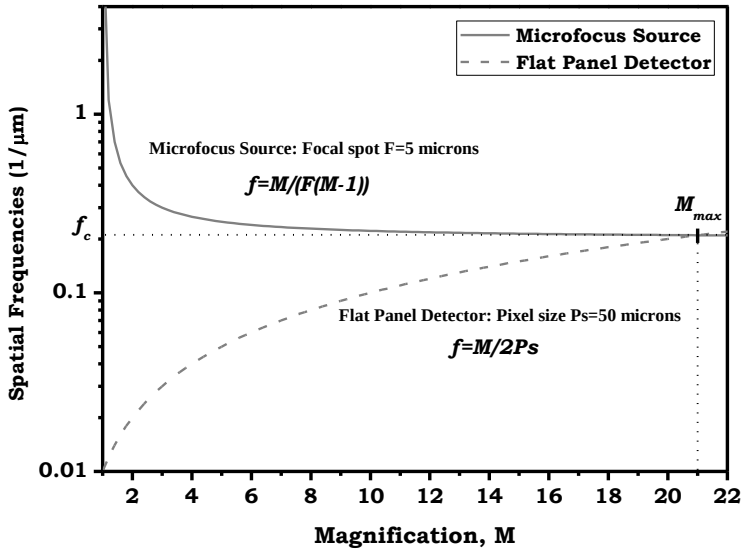

Figure 3. System cut-off frequency assuming 5 microns spot size microfocus source and 50 microns pixel size detector

It can be appreciated how the cut-off frequency found for a magnification factor is equal to 21; over this value the blurring effects dominate. This value for *M* corresponds to a distance *OS* of 23.8 mm, an effective pixel size of 2.4 microns and a field of view of 5.7 mm. The particularly selected source presents a focus to object distance (FOD), i.e. distance from the target to the nearest point out of the beryllium window) of 6.8 mm, that means an object at that magnification needs to be at 17 mm of the external beryllium window. The cut-off frequency represents the optical limits under ideal conditions although real resolution might be limited by other factors.

In this sense, the ability of any imaging set-up to transfer an object into image is more realistically described by the modulation transfer function (MTF) since MTF considers both spatial and contrast resolution at the same time. Nominally a value of MTF for any imaging set-up is assigned at 10% of the maximum MTF. The value found for this detector at M = 1 using a resolution target mod 07-553 from Nuclear Associates is approximately 10 lp/mm (line pairs per mm) that corresponds to 50 microns, i.e. current pixel size of the detector [30]. This means that the assumption of 50 microns pixel size used for the cut-off frequency calculations in figure 3 is valid for this particular set-up.

On the other hand, it must be considered that contrast in the MTF targets is high since high absorbing elements, typically Mo, are used to create the pattern. Therefore it is expected that in the case of low absorbing materials such as polymers and cellular polymers, the final resolution will be slightly limited by the lower absorption (lower image contrast) of these materials. In this sense, the image quality in terms of contrast depends on the experimental conditions as follows:

- Radiation conditions: Aiming optimum contrast, X-ray energy must be rather low (polymers present higher absorption at lower energies). Nevertheless, as mentioned, the detector response might be insufficient, so in order to compensate this insufficient detector signal it is recommended to use high X-ray intensities (photon flux).

- Exposure time: Similar to the increase of X-ray intensities it is recommended to use higher than usual exposure times in the detector (as an example double exposure time implies double number of photons i.e. double signal since linearity of these detector is very good). Recommended acquisition time for this kind of materials is in the range 1-3 seconds, thus, limiting time resolution that needs to be slightly over these values.

-Type of material and thickness: As known, X-ray absorption coefficient, μ, depends on the density and the elements present (Z number) in the irradiated object [31]. Polymers are mainly constituted by light elements: C, O, H and less frequently F, S, P, Cl, etc, thus the presence of light elements makes most of polymers almost X-ray transparent and in the case of low density cellular polymers the effective absorption is much lower as density is reduced (up to few percent of initial solid polymer for a same thickness). On the other hand, according to Beer-Lambert equation (see eq. 2) thickness, *t*, will also play a fundamental role in the image contrast and correlates exponentially with the transmitted intensity.

$$I = I_0 \cdot e^{-\mu t} \qquad (2)$$

Over the mentioned influencing parameters on image quality, last can be further improved by means of analogue integration procedure, but of course loosing time resolution. This noise-reducing methodology consists in acquiring the same image consecutively (generally up to 16 times). The image integration contributes to reduce the natural noise (random nature) of the detector thus defining better those poor-contrast parts.

Time resolution can be improved by another special procedure called pixel binning. This procedure collects the energy of 2 x 2 or 4 x 4 pixels at once and therefore the required exposure time for similar pixel intensity is 0.25 or 0.125 times of the original respectively. The handicap of this procedure lies in the reduction of the original spatial resolution accordingly to the pixel binning applied. Integration and binning procedures are frequently used in digital imaging although not all detection systems allow for them. Our particular system allows for both of them and its maximum acquisition velocity is limited up to 9 fps at 4x4 binning conditions.

2.3 Image correction

Another, usually not-mentioned, aspect is the necessity of image correction. Original images taken inevitably contain unevenness of dark offset, non-uniformity of X-ray intensity distribution, blemish of scintillating material and few defect pixels. Therefore, correction is a typical procedure in digital imaging and particularly necessary in the case of X-ray digital imaging with flat panel detectors. The correction is carried out by a two-step process that computes the image together with two additional correction images, called darkfield and flatfield, previously acquired. Correction process is automatically done by the HiPic software used.

Prior to the image correction, defective pixels have been identified thanks to a special module in HiPic. Defect pixel masking eliminates the information from those dead or hot pixels and assigns an interpolated value based on the intensity collected by the surrounding pixels. After defect pixel correction the pixel value is not acquired and directly interpolated so input image already contains this correction.

The first step of image correction consists in a background subtraction process, thus the darkfield image (also called background, i.e. an image without X-rays at the same exposure time) is subtracted from the one intended to be corrected. Noise in the taken background images can be reduced by image integration procedure although intensities need to be normalized then by the number of integrations. The background-subtracted intensity, $I_{BS,}$ of each pixel can be calculated as difference of the pixels in the original image, $I(x,y)$, and the ones in the darkfield , $I_d(x,y)$ as shown in eq. 3:

$$I_{BS}(x,y) = I(x,y) - I_d(x,y) \qquad (3)$$

Secondly, flatfield correction basically corrects the varying sensitivity within the full detector area as well as spatial non-uniformity of the X-ray source, aiming to obtain homogeneous intensity in the whole area, i.e. similar intensity in all the pixels. Flatfield image is acquired at similar conditions (kV, μA, SD distance and exposure time) that the radiography to be corrected. Integration for noise reduction is done similarly as for the darkfield. Correction procedure implies the calculation expressed in eq. 4 , with $I_f(x,y)$ the intensity of the individual pixels in the flatfield image:

$$I_{FC}(x,y) = \bar{I} \cdot \frac{I_{BS}(x,y)}{I_f(x,y) - I_d(x,y)} \tag{4}$$

and $\bar{I}$ the average intensity of $I_f(x,y) - I_d(x,y)$ *through the whole panel.*

Darkfield and flatfield correction images need to be periodically updated to preserve image quality considering that dark offset and sensitivity evolve with time.

.

3. Application for density determination:

3.1 Calculations based on Beer-Lambert equation

As it was mentioned at the beginning, the X-ray attenuation is an exponential function of the mass attenuation coefficient of the material (single element), μ, and its thickness, t. Thus, the transmission is accurately predicted by the mentioned Beer-Lambert expression (eq. 2)

Nevertheless, the mass absorption coefficient is not a constant and depends on the incident energy of the beam. So, strictly talking, this expression is only valid for a monochromatic beam. A similar expression predicts the attenuation in the case of incident multispectral X-ray beam (so-called *white beam or bremsstrahlung*) by substituting the attenuation coefficient by the effective multispectral one, $\overline{\mu}$. This approximation is valid for an element with a thickness low enough that beam hardening effect is not present, so selected energies are not absorbed.

Similarly, if the material is constituted by diverse elements the absorption coefficient is a weighted average of their individual multispectral absorption coefficients (μ_i) and their concentrations (c_i) if, again, beam hardening is not predominant:

$$\overline{\mu}_{eff} = \sum_i c_i \cdot \overline{\mu}_i \tag{5}$$

In the particular case of a cellular material it is valid to assume the behaviour of a bi-component system, therefore the effective absorption coefficient can be described as

$$\overline{\mu}_{eff} = c_{air} \cdot \overline{\mu}_{air} + (1 - c_{air}) \cdot \overline{\mu}_{solid} \tag{6}$$

Therefore by having two reference intensities, $I_{REF\text{-}i}$ *(i = 1, 2)*, in strict correspondence with two known concentrations (i.e. two known reference densities) it is possible to calculate the porosity at any point of the material, $c_{air}(x,y)$, through the projected intensity, $I(x,y)$, in the radiography through eq. 8.

$$I_{REF-i} = I_0 e^{-[c_{REF-i}\mu_{air} + (1-c_{REF-i})\mu_{solid}]t} \tag{7}$$

$$c_{air}(x,y) = c_{REF-1} + \frac{\ln \frac{I_{REF-1}(x,y)}{I(x,y)}}{\ln \frac{I_{REF-1}}{I_{REF-2}}} (c_{REF-1} - c_{REF-2}) \tag{8}$$

The two used references for the spatial density determination are commonly:

i) A region in the radiography with no material (air, 100 % porosity)

ii) The average intensity within the area occupied by the bulk material (bulk density of the foam). Alternatively, it is possible to use a solid precursor with a same thickness as the

reference intensity value for the 0 % porosity and, thus, calculating the density at any point without knowing the bulk density of the material examined.

For the sake of illustration figure 4 shows a radiograph (left) and the density profile (right) obtained from the dashed region depicted in the left figure. The density determination was done by using the background and the average grey level in the foam as known references (air and bulk/average already known densities). It can be observed a clear parabolic profile for XPS foam obtained by extrusion with a thin, denser outer skin of roughly 0.2mm. The obtained curve is rather smooth along the profile.

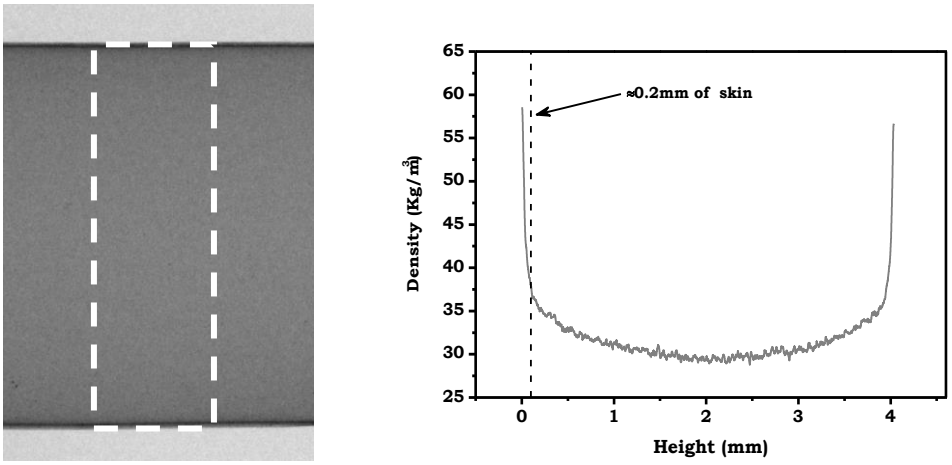

Figure 4. Radiography (left) and calculated vertical density profile (right) of a foam with average density 32 kg/m^3. White dashed region is the one from which the vertical profile was calculated.

3.2. Additional considerations

The method described above considers a constant sample thickness, *t*, nevertheless the cone beam may induce some distortions on this value. These distortions are calculated in this section based on the scheme of Figure 5.

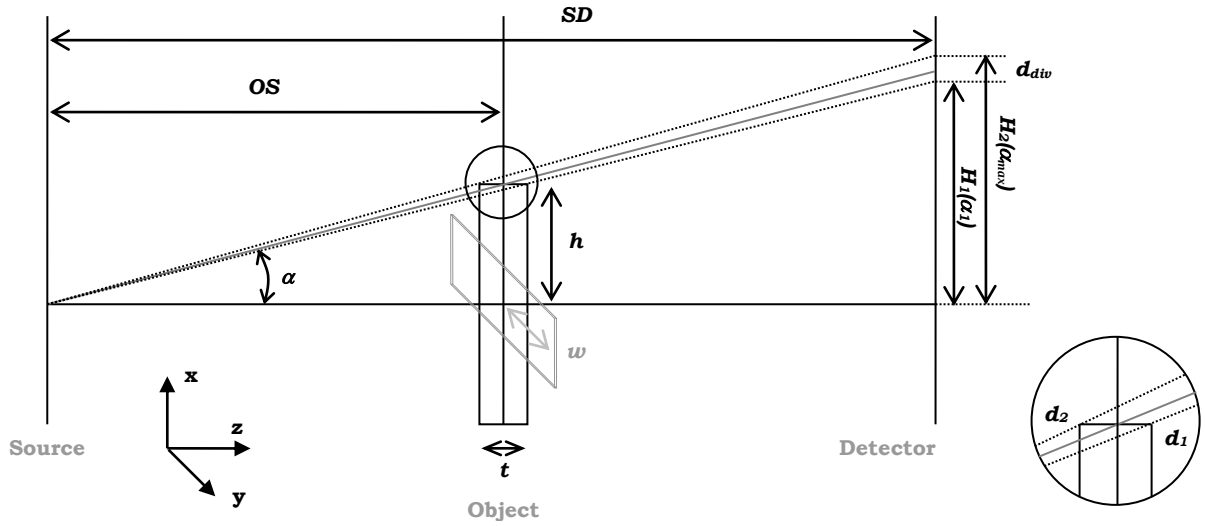

Figure 5. X-ray imaging projection geometry.

According to figure 5, the cone beam divergence produces two main (but generally minor) effects:

-*Effective thickness increase*: out of the centre of the image the beam path slightly increases in comparison with the orthogonal direction. Effective thickness, *t´*, is then a function of the distance to the centre (*x*) and can be corrected by a factor C_1. Therefore, according to trigonometric calculations the effective thickness can be expressed as:

$$t' = t \cdot C_1 \text{ with } C_1 = \frac{1}{\cos\left(arctg\left(\frac{x}{OS + t/2}\right)\right)} \text{ valid only for } \alpha \le \alpha_1,\ \alpha_1 = arctg\left(\frac{h}{OS + t/2}\right) \tag{9}$$

Although, alternatively, it might be proper to better express it as a function of the magnified projected distance to the detector centre, *X*, i.e. distance to the image centre:

$$t' = t \cdot C_1 \text{ with } C_1 = \frac{1}{\cos\left(arctg\left(\frac{X}{SD}\right)\right)} \text{ valid only for } H \le H_1,\ \mathrm{H}_1 = h \cdot M_1 = h \cdot \frac{SD}{OS + t/2} \tag{10}$$

-*Edge distortion*: Just at the extreme end of the object, the effective thickness is reduced, then at any *X* region in between H_1 and H_2, the effective thickness can be calculated as:

$$t' = t \cdot C_2 \text{ with } C_2 = \frac{d}{\cos\left(arctg\left(\frac{X}{SD}\right)\right)} \text{ valid only for } H_1 < X < H_2,\ \mathrm{H}_2 = h \cdot M_2 = h \cdot \frac{SD}{OS - t/2} \quad (11)$$

with *d* equal to:

$$d = d_1 - d_2 = \left(\frac{h}{tg(X/SD)}\right) - (OS - t/2) \quad (12)$$

In which d_2 is a constant and d_1 varies in the range (d_2, d_2+t) and, therefore, *d* varies in between 0 and *t*.

The region in between H_1 and H_2 is also called *divergence distortion*, d_{div} [23], and can be estimated (assuming $t << OS$) as:

$$d_{div} = hM_2 - hM_1 = h\frac{SD}{OS - t/2} - h\frac{SD}{OS + t/2} = h \cdot t\frac{SD}{OS^2 + t^2/4} \cong \frac{h \cdot t}{M \cdot OS} \quad (13)$$

It is important to mention that divergence distortion is of different nature of penumbra region caused by finite size of focal spot size already mentioned before.

Current Cartesian 2D reference system chosen is coherent with digital detector arrangement; therefore the correction for an object of dimensions *h* –height– and *w* –width– can be carried out over any generic pixel value (X,Y), with already known distance to the centre of the image, by only inputting sample thickness and current magnification (or *OS* and *SD* distances).

For sake of illustration, figure 6 shows as an example the calculated normalized effective thickness, C_1 and C_2 as continuous function, for objects with different thickness (*t* = 5, 10 and 20 mm) and height *h* = 30 and 15 mm situated at positions such that the magnification factors (M) are 2, 4 and 8 times. Note that in the graph, due to different ranges covering C_1 and C_2 a scale brake has been used, thus C_1 is shown in the top part of the graph and C_2 mainly in the bottom part of the graph. The apparent discontinuity of C_2 is due to the scale break and the different resolutions of bottom and top scales.

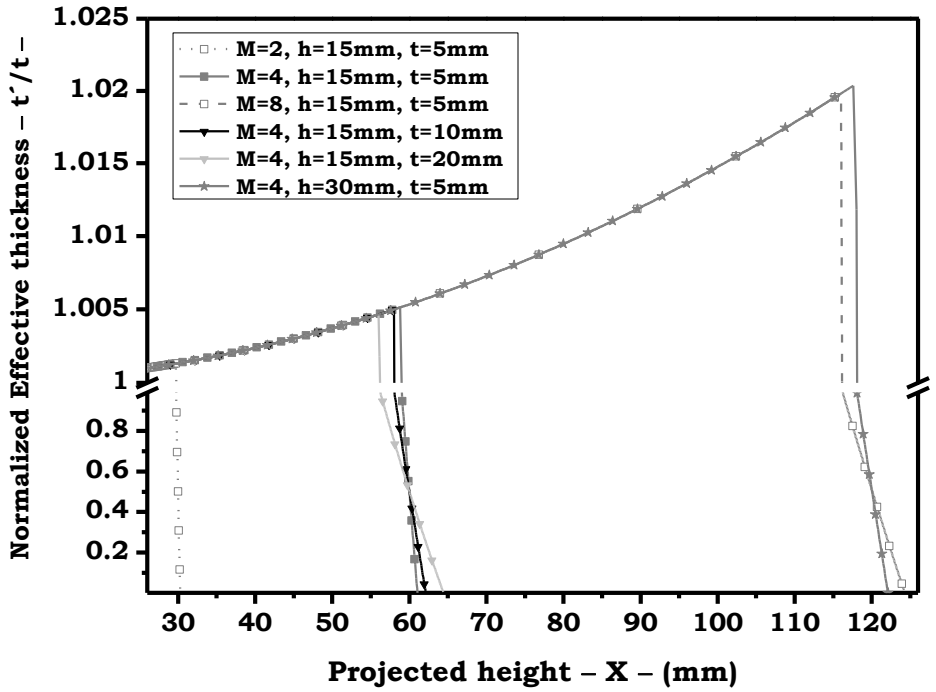

Figure 6. Normalized effective thickness for objects of different thickness and size located at different magnification positions

Figure 6 shows how the normalized effective thickness increases progressively while separating from the centre of the image. Theoretical projected heights have been computed in fig. 6 to be up to 120 mm although, according to the scheme, the maximum projection for a 120 x 120 mm^2 detector is a half-diagonal of 85 mm. The effect of effective thickness increase along the projected height bellow H_1 is independent from thickness, magnification or sample height. On the other hand the divergence distortion region actually depends on all sample thickness and height as well as magnification.

3.3 Limitations of the method

It is obvious that the mentioned procedure presents certain limits in terms of accuracy for the density determination. Therefore error and precision of the obtained density will depend on diverse factors.

Probably one of the most important limitations is the obvious relationship in between the dynamic range of the detector and the precision in the density determination. In a first approach, a 12 bit output expresses, potentially, 4096 intensity levels to be correlated with density. Nevertheless, for a

certain object the particular gray-scale covering the transmitted intensities of that object is restricted to a reduced grey level range (see figure 7-b). In this sense, the number of gray levels covering the density "spectrum" is related to the acquisition parameters (voltage, current and exposure time) that need to be optimized depending on both the material characteristics (foam density, polymer type and thickness). Therefore the contrast associated to a certain material is a competition in between the absorption/transmission and the detector response. Particularly the detector response always increases at higher energies/intensities (shown in fig. 1) whereas the transmittance decreases with energy [32]. As a result the contrast does not monotonically increase with X-ray energy and it is difficult to find the optimum imaging parameters, specially the optimum tube voltage, for a specific material and thickness. Based on eq. 2, it is possible to find the optimum kV after choosing a certain transmittance criterion. In our particular case we have chosen $T = I/I_0 = 0.135$, according to which was reported by Grodzins [33].

Table 1 shows the optimum monochromatic energy calculated for diverse polymeric materials for t = 2 mm of solid material (20 mm of a foam with 10 % of relative density) and $T = I/I_0 = 0.135$ from eq. 2. Please note for a polychromatic tube emission (bremsstrahlung, as in our case) the emitted kV is, properly talking, the maximum energy of the emitted spectrum, kVp, Therefore, in practice the average energy emitted is significantly lower than kVp and kVp is only a small fraction of the total emitted energy spectrum.. From results in table 1 it can be appreciated how the optimum energies for polymers under the specified conditions are lower than the minimum energies that the tube can emit, 20 kV although, on the other hand the detector response at such low energies would be insignificant. As a compromise higher energies are used.

Table 1.

Calculated optimum energies for different 2mm-thick solid polymers and aluminium under the $T = 0.135$ criterion.

material	**$kV_{opt.}$ (Exp.)***	**$kV_{opt.}$ (Th.)****
PE (C_2H_4)$_n$	5.88	5.62
PP (C_3H_6)$_n$		5.66
PS (C_8H_8)$_n$	6.00	6.09
PC ($C_{16}H_{14}O_3$)$_n$		6.98
PMMA ($C_5H_8O_2$)$_n$	7 aprox	7.28
PI ($C_{22}H_{10}N_2O_5$)$_n$		7.59
PTFE (C_2F_4)$_n$	9 aprox	11.21
Aluminium (Al)	13.88	18.97

*μ interpolated from[34]; **T obtained from [32]

An illustrating example of comparative grey-scale precisions is depicted in figure 7 for three PE slab-shaped foamed materials of different thicknesses. The foams are obviously represented by different grey level ranges depending on their thickness (contrast in the images has not been individually optimized and only for the three materials simultaneously, accordingly to the diagonal line in figure 7-b). Apart from the average grey level shift, the representative histogram presents distinctly different shape (width, height) for the different materials under similar imaging parameters. Particularly in the example of figure 7 the full width at half-maximum (FWHM) representing the different materials is 19.3, 15.5 and 14.1 for thicknesses of 2, 1 and 0.5 mm respectively.

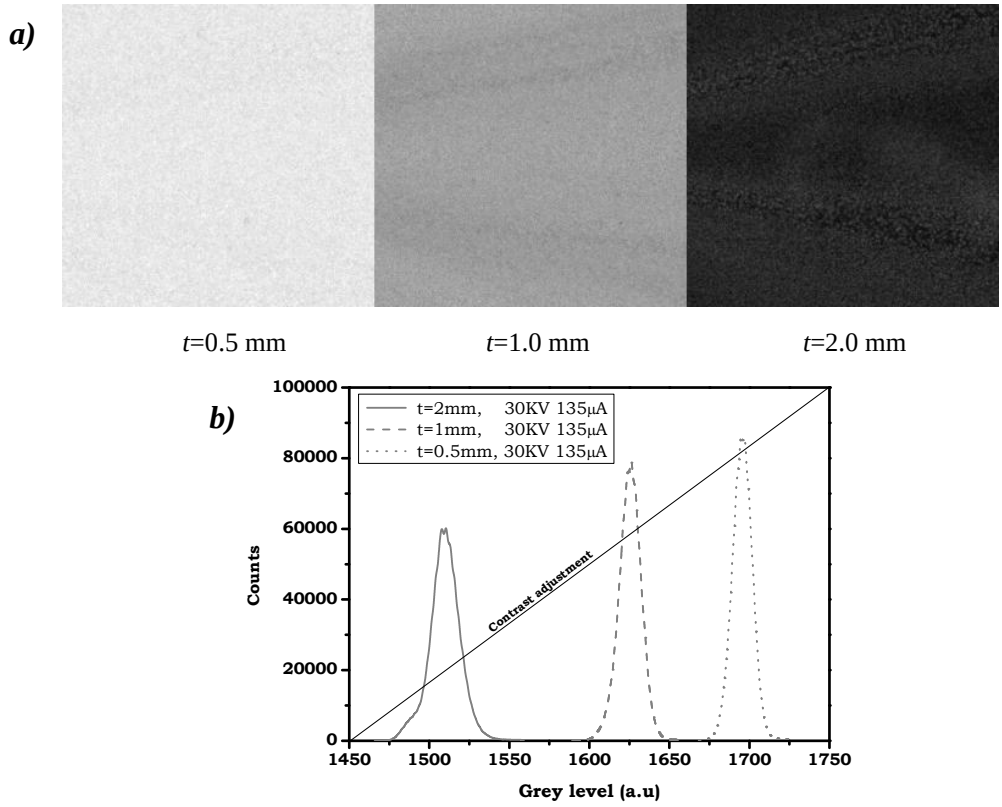

Figure 7. a) Zoomed radiographies of injected polypropylene slabs of 0.5, 1 and 2 mm with 18% porosity,(from left to right),
b) Grey level histograms of the regions visualized in fig.7a).

From these results we can confirm that not only the acquisition parameters but also the characteristics of the studied sample (thickness, polymer type and/or relative density) influence the imaging results. In general, excessive or too low energies/intensities may cause a reduction in the number of grey levels contained within the acquired image, later associated to density levels.

Figure 8 shows the different histograms obtained under different X-ray energies and intensities. It is possible to observe that the increasing energy/intensity causes a broadening in the characteristic histogram, thus, offering better precisions (levels contained in the histogram) for the density determination. The observed fact is, in this particular case, associated to a better detector response versus the competitive transmittance reduction. Therefore, it would be expected that the histogram becomes narrower (contrast resolution reduces) at a certain energy over 40 kV .

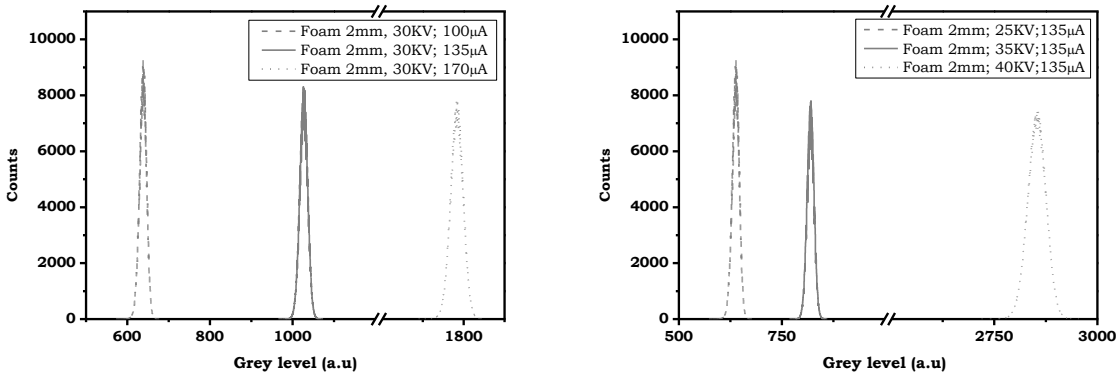

Figure 8. Characteristic histograms obtained for a sample of thickness 2 mm and 12% porosity, under different intensities (left) and different kV_p (right).

Apart from the necessity of a fine adjustment of the imaging parameters depending on the sample characteristics, it is necessary to take into account several spurious effects that may affect the resolution in density. Among others, we can mention the *effective thickness increase* (discussed in section 3.2), the natural noise in the detector (SNR) and the thickness in-homogeneity in the beam direction. In principle the effect of effective thickness slightly tends to broaden the histogram in its low grey-level region. This is evident in fig-7-b for the sample thickness t = 2 mm, which histogram curve presents a negative asymmetry influenced by this factor. This "tail" is less evident for thinner materials, as expected, but still remains. On the other hand, as soon as SNR reduces, the Gaussian distribution would tend to broaden.

Effect of thickness in-homogeneity mainly non-constant thickness throughout the sample could be, in principle, dismissed having only significant influence when it is really high. An angle deviation of the normal vector to the slab material with respect to the beam direction may also produce small errors in the density determination due to different effective thickness in the XY plane but will also be not considered here. Lastly we will consider no effect of beam hardening since it is negligible for these type of measurements and materials.

Under authors´ point of view, the FWHM is the parameter that better expresses the potential resolution of the acquire image, although it is difficult to assign an absolute precision for the density determination. This value is quite independent from the edge distortion and noise artefacts under the considerations mentioned above. The FWHM value is quite conservative if it is direct related to density resolution because it only considers the resolution for individual pixels values.

Nevertheless, it is possible to obtain finer resolution (intermediate values) by averaging surrounding pixels. As an example in a vertical profile (X direction) a certain number of pixels in the Y direction can be considered and averaged providing a finer precision for each individual value in the X direction (See Fig. 4).

4. Other potential applications of the technique:

The intensive revision of the hardware, the method and the factors involved in the image quality as well as its quantitative evaluation given in this paper is now completed with a brief overview on the possible applications of this technique for the study of cellular materials. Probably one of the most known/expected applications for X-ray nondestructive testing apparatus is the use of such technique for the analysis of defects and in-homogeneities in produced materials as quality control [35]. Fig. 10-A- shows an example of a PE foam produced with evident density inhomogeneities, illustrating this application. Figs 10-B- and 10-C- show other types of defects such as microporosity in the skin of an integral PP foam and gas entrapments in the cellular structure of a rigid PU foam. In general, this type of analysis does not associate quantification and the image is simply used for visual inspection, aiming diverse objectives. Among others, radiographies are particularly useful for the inspection of prototypical parts [35], both to know about the sample quality and to elucidate how it was developed while processing (example, flux lines, typical of injection moulding process). X-ray analysis can be also applied to study failing/defective components or already mechanically tested ones with the objective of knowing more about the internal structure in the surroundings of the failing area.

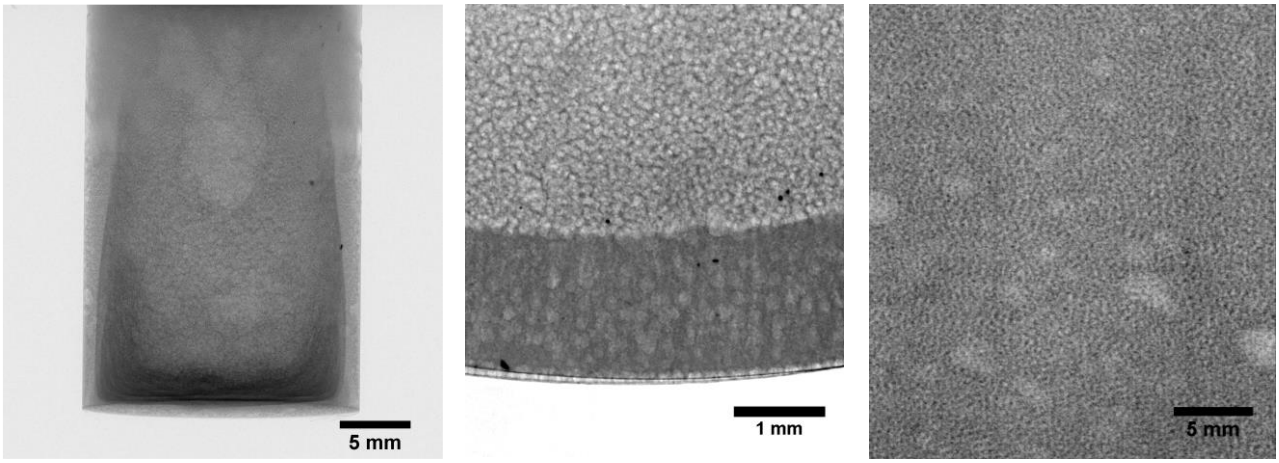

-A- -B- -C-

Fig 10. -A- Radiography of an in-homogeneous non-crosslinked PE foam cylinder.
-B- Microporosity present in the skin of a integral PP foam
-C- Gas entrapments in a rigid PU foam of density 180Kg/m^3

A second possible application based on radiography is the determination of diverse structural parameters such as density profile, skin thickness [36] or the approximate cell size [37]. These types of determinations involve the extraction of numerical variables from the image. The variables can

be associated simply to dimensional aspects of the image (sizes, i.e. distances) or related to the intensity value of the radiography (converted to density afterwards). Furthermore, it is possible to combine the pixel value and the pixel position creating density profiles or 2D maps. Fig 4 illustrates an example on this application type where both density profile and skin thickness could be determined. Fig 10-b, shows a clear example on the possibility of dimensional quantification since from the radiography it is possible to extract the skin thickness and even the average porosity of that region.

Nevertheless, by far, the X-ray equipment described here offers its best compliance in the particular case of in-situ studies, i.e., monitoring the sample evolution while foaming by means of sequences of radiographies, the so called radioscopy method [38]. With this methodology it is possible to carry out the analysis of physical mechanisms taking place during foaming for both thermoplastics and thermosets materials. Therefore, under special setting up conditions (X-ray transparent furnaces and/or moulds) it is possible to on-line monitor the dynamics of cellular structure and calculate the cell wall rupture rate [39], determine density profiles [23], monitor the rupture speed of a cell wall using ultrahigh speed radioscopy in a synchrotron [4] and/or characterize the macroscopic expansion [23].

Images in fig. 11 show the expansion and cellular structure evolution of rigid PU foam (BASF, polyol A-component Elastopor® H 1501/1,isocyanate B-component IsoPMDI 92140) growing in a paper mould of Ø=16mm. Based on final density of the sample the density evolution can be accurately calculated. Furthermore the pore size evolution can be roughly discriminated.

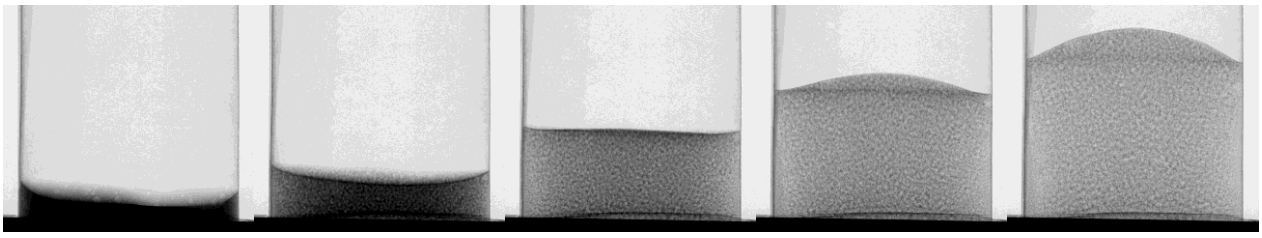

Fig 11. Series of radiographs obtained during an in-situ radioscopic experiment of a rigid PU foam during its expansion at times 0, 30, 60, 90, 120 seconds.

5. Conclusions

X-ray techniques based on a microfocus/nanofocus X-ray tube in combination with a high resolution and high sensitivity detector offers multiple and unique advantages for the study of polymeric foams in comparison with conventional methods:

- It is a non-destructive technique with a high spatial resolution (down to 1 micron, if a nanofocus tube is used).
- There is no depth of field limitations, the specimen is imaged sharply throughout its entire depth.
- The penetration is high and tuneable though the sample. It is possible to appreciate inner parts.
- Suited both for still imaging (already produced foam parts) and in-situ experimentation (during the production process). It is even possible setting up small adapted furnaces in between the tube and the detector which powers up the system flexibility to monitor any phenomena taking place in the mould.
- The system allows continuous variable magnification which gives great flexibility to the system.
- In general, sample preparation is not necessary, although for the visualization of some particular features it might be necessary
- Using proper methodologies it is possible to extract quantitative information from the images (density profiles, size and shape of defects, cell size, local expansion ratio, etc)
- The system is compatible with the possibility of obtaining 3D information of the foam structure –via performing X-ray microtomography- by using a rotating table with the axis suitable adjusted.

Nevertheless not all the X-ray systems are identical. Particularly microfocus X-ray systems are distinctly different from synchrotron X-ray facilities, although both can be potentially used for the study of polymer foam systems. In principle, the laboratory systems offer a daily use availability, much less cost per working hour and significant larger field of view but, in contrast, synchrotron X-rays are “premium quality”, with orders of magnitude higher photon flux, parallel beam configuration, higher spatial resolution and the possibility of using tunable monochromatic X-rays which enables multiple working modes [40].

The specific system presented in this paper has been designed to be used with low X-ray absorbing materials. The high sensibility of the detector which provides better image contrast is one of the critical parameters in the system. The examples and explanations given in the paper show the potential of the method. In addition the key methodologies that it is necessary to set-up in order to

obtain images with high quality and to extract quantitative and precise information have been described in detail.

From the revision of the literature it is clear that the potential of X-rays applied on the study of polymeric foams has been, still, scarcely used (with exception of X-ray tomography). Nevertheless, it is expected researchers to extensively use this technique in the following years to understand phenomena related to foam physics in polymeric and aqueous foamed systems.

6. References

[1] L. Cartz. Nondestructive Testing. A S M International. 1995

[2] C. Hellier. Handbook of Nondestructive Evaluation. McGraw-Hill. 2003

[3]. S. A. Wenk, R.C. McMaster. Choosing NDT: Applications, Costs and Benefits of Nondestructive Testing in Your Quality Assurance Program. American Society for Nondestructive Testing. 1987.

[4]. A. Rack, F. García Moreno, T. Baumbach, J. Banhart. Synchrotron-based radioscopy employing spatio-temporal micro-resolution for studying fast phenomena in liquid metal foams. J Synchrotron Radiat 2009; 16(3): 432–434

[5] S. Youssef , E. Maire, R. Gaertner. Finite element modelling of the actual structure of cellular materials determined by X-ray tomography. Acta Mater 2005; 53(3): 719-730

[6] J. Adrien ,E. Maire, N. Gimenez, V. Sauvant-Moynot. Experimental study of the compression behaviour of syntactic foams by in situ X-ray tomography. Acta Mater 2007; 55(5): 1667-1679

[7] A. Elmoutaouakkil, G. Fuchs, P. Bergounhon, R. Péres, F. Peyrin. Three-dimensional quantitative analysis of polymer foams from synchrotron radiation x-ray microtomography. J Phys D Appl Phys 2003; 36(A37)

[8] M. D. Montminy, A. R. Tannenbaum, C. W. Macosko. The 3D structure of real polymer foams. J Colloid Interf Sci 2004; 280(1): 202-211

[9] P. Babin, G. Della Valle, R. Dendievel, D. Lourdin, L. Salvo. X-ray tomography study of the cellular structure of extruded starches and its relations with expansion phenomenon and foam mechanical properties. Carbohyd Polym 2007; 68(2): 329-340

[10] S. Roux, F. Hild, P. Viot, D. Bernard. Three-dimensional image correlation from X-ray computed tomography of solid foam. Compos Part A-Appl S 2008; 39(8): 1253-1265

[11] M. Di Michiel, J. M. Merino, D. Fernandez-Carreiras, T. Buslaps, V. Honkimäki, P. Falus, T. Martins, O. Svensson. Fast microtomography using high energy synchrotron radiation. Rev. Sci. Instrum. 2005; 76: 043702

[12] R. J. Jennings. J Cell Plast 1969; 5: 159-172

13] R. L. Rowton. J Cell Plast 1980; 16: 287-292.

[14] A. Van Thuyne, B. J. Zeegers. J Cell Plast 1978; 14: 150-160.

[15] Y. Jianqiu, Z. Jianyaun, W. Dening, H. Chumpu, Y. Shengkang, C. Yiou, C. Yufu,X. Ziqian , S. Jin, W. Yin. J Cell Plast 1990; 26: 39-49

[16] J. I. Velasco, M. Antunes, O. Ayyad, C. Saiz-Arroyo, M. A. Rodríguez-Pérez, F. Hidalgo, J. A. de Saja. J Appl Polym Sci 2007; 105: 1658-1667.

[17] J. I. Velasco, M. Antunes, O. Ayyad, J. M. López-Cuesta, P. Gaudon, C. Saiz, M. A. Rodríguez-Pérez, J. A. de Saja. Polymer 2007; 48: 2098-2108.

[18] E. Solórzano, M. Antunes, C. Saiz-Arroyo, M.A. Rodriguez-Perez, J.I. Velasco, J.A. de Saja. Optical Expandometry: A Technique to Analyze the Expansion Kinetics of Chemically Blown Thermoplastic Foams. J Appl Polym Sci (in press, 2011)

[19] Q. Guo, J. Wang, C. B. Park, M. Ohshima. A Microcellular Foaming Simulation System with a High-Pressure Drop Rate. Ind Eng Chem Res 2006; 45(18): 6153-6161,

[20] T. G. Cunningham, S.C. Graham. Imaging the internal structure of Bulk Materials by Microfocal Radiography. Materials and Design 1986; 7: 223-231

[21] J. Banhart, H. Stanzick, L. Helfen, T. Baumbach. App Phys Let 2001; 78:1152-1154

[22] J. Banhart, H. Stanzick, L. Helfen, T. Baumbach, K. Nijhof. Real-time X-ray investigation of Aluminium Foam Sandwich production. Adv Eng Mater 2001; 3: 407–411

[23] F. García-Moreno, M. Fromme, J. Banhart. Real-time X-ray Radioscopy on Metallic Foams Using a Compact Micro-Focus Source. Adv Eng Mater 2004; 6: 416-420

[24] F. García-Moreno, N. Babscan, J. Banhart. X-ray radioscopy of liquid metal foams: influence of heating profile, atmosphere and pressure. Colloid Surface A 2005; 263(1-3): 290–294

[25] N. Babcsán, F. García-Moreno, J. Banhart. Metal foams - High temperature colloids. Part II: In-situ analysis of metal foams. Colloid Surface A 2007; 309(1-3): 254–263
[26] F. García-Moreno, C. Jiménez, M. Mukherjee, P. Holm, J. Weise, J. Banhart. Experiments on metallic foams under gravity and microgravity. Colloid Surface A 2009; 344(1-3): 101–106
[27] M. Mukherjee, F. García Moreno, J. Banhart. Defect generation during solidification of aluminium foams. Scripta Mater 2010; 63(2): 235–238
[28] O Brunke, S Odenbach. In situ observation and numerical calculations of the evolution of metallic foams. J Phys Condens Matter 2006; 18: 6493
[29] A Myagotin, L Helfen, T Baumbach. Coalescence measurements for evolving foams monitored by real-time projection imaging. Meas Sci Technol 2009; 20: 055703
[30] A. Sisniega, J. J. Vaquero, E. Lage, A. de Carlos, J. L. Villena, M. Abella, I. Vidal, G. Tapias, J. C. Antoranz, M. Desco. Comparative Study of Two Flat-Panel X-RayDetectors Applied to Small-Animal Imaging Cone-Beam Micro-CT. IEEE Nuclear Science Symposium Conference Record 2008
[31] J. Banhart, A. Borbély, K. Dzieciol, F. García-Moreno, I. Manke, N. Kardjilov, A.R. Kaysser-Pyzalla, M. Strobl, W. Treimer. X-ray and neutron imaging - Complementary techniques for materials science and engineering. Int J Mater Res 2010; 101(9): 1069–1079 (2010)
[32] http://henke.lbl.gov/optical_constants/filter2.html (January 2012)
[33] L. Grodzins. Optimum energies for X-ray Transmission tomography of small samples, Application of synchrotron radiation to computerized tomography I. Nucl Instrum Methods 1983; 206: 541-545
[34] http://www.nist.gov/pml/data/xraycoef/index.cfm
[35] D. Mery, D. Filbert. Automated Flaw Detection in Aluminum Castings Based on the Tracking of Potential Defects in a Radioscopic Image Sequence. IEEE T Robotic Autom 2002; 18(6)
[36] J. Pinto, S. Pardo, E. Solorzano, M. A. Rodriguez-Perez, M. Dumon, J. A. de Saja. Solid skin characterization of PMMA/MAM foams fabricated by gas dissolution foaming over a range of pressures. Defect Diffus Forum (in press 2012)
[37] S. Pardo, S. Estravís, E. Solórzano, M.A. Rodríguez-Pérez, J.A. de Saja. Effect of Nanoadditives in Rigid Polyurethane Foam Nucleation Monitored by X-ray Radioscopy, Proceedings of the SPE Eurotec® Conference, 2011
[38] F. Garcia-Moreno, M. Mukherjee, C. Jiménez, A, Rack, J. Banhart. Metal Foaming Investigated by X-ray Radioscopy. Metals 2012; 2(1): 10-21
[39] F. Garcia-Moreno, E. Solórzano, J. Banhart. Kinetics of Coalescence in Liquid Aluminium Foams. Soft Matter 2001; 7: 9216-9223
[40] J. Banhart. Advanced tomographic methods in materials research and engineering. Oxford University Press 2008.